



THEORETICAL CALCULATIONS OF THE COLLECTION EFFICIENCY OF SPHERICAL PARTICLES AND FIBERS IN AN IMPACTOR

Bahman Asgharian,*† Lei Zhang* and Ching Ping Fang‡

*Chemical Industry Institute of Toxicology, P.O. Box 12137, Research Triangle Park, NC 27709, U.S.A.

†Department of Environmental Medicine, New York University Medical Center, New York, NY 10016, U.S.A.

(First received 29 March 1996; and in final form 14 June 1996)

Abstract—Collection efficiencies of two types of impactor nozzles were calculated for spherical particles and fibers. The flow field through the impactor was calculated for Reynolds numbers of 100 and 1100 using a finite element method. Equations of motion for spherical particles and fibers were obtained and were used along with flow field information to calculate impactor collection efficiencies. The calculated collection efficiency for spherical particles agreed with that in the literature. The cutoff size at 50% agreed with experimental data, but the collection efficiency curve lacked a long tail at low collection efficiencies. For fibers, collection efficiency curves were obtained in terms of fiber Stokes number and aspect ratio. The calculated collection efficiency curve moved to higher Stokes numbers with increasing fiber aspect ratio. The cutoff size for fiber minor diameter decreased as the fiber aspect ratio increased. Copyright © 1997 Elsevier Science Ltd

1. INTRODUCTION

Well-characterized particles and fibers are desirable in many applications, including inhalation toxicology where deposition and clearance of materials in the lung depend on their physical properties. One method for separating large materials is by their inertia. Many types of impactors have been constructed and evaluated for this purpose.

Numerous attempts have been made to predict the characteristic behavior of impactors. Early theoretical works were based on simplified flow fields (Davis and Aylward, 1951; Ranz and Wong, 1952; Wilcox, 1953; Mercer and Chow, 1968; Mercer and Stafford, 1969) that led to only approximate calculations of collection efficiency. Particles used in these studies were assumed to be spherical. More accurate flow fields were found by Marple (1970) and Marple *et al.* (1974) by using a finite difference scheme to solve the flow field numerically. While experimental measurements exhibit an S-shaped curve for collection efficiency plotted against the square root of the Stokes number, theoretical predictions lack a tail in the low end of the collection efficiency curve. Improvement on the theoretical model (Rader and Marple, 1985) and better selection of particle size in experimental studies (Wang and John, 1988; Hillamo and Kauppinen, 1991) did not resolve the discrepancy in the collection efficiency curves. Despite differences in the shape of the collection efficiency curve, the cutoff size of the particles at 50% efficiency is in good agreement between theory and experiment.

Most particles are not spherical. Impactors have been used to separate nonspherical particles by their aerodynamic diameters. This method of separation is valid only when the shapes of the particles do not significantly deviate from spherical geometry. Aerodynamic diameter depends on the flow field and geometry of the device in which it is measured (Yu *et al.*, 1986). Esmen and Erdal (1991) found that nonspherical particles do not have a unique aerodynamic diameter. The appropriate diameter in an impactor is called the impaction diameter (Yu *et al.*, 1986). For fibers that have a well-defined geometry, a collection efficiency curve as a function of the physical dimensions of the fibers can be obtained.

† To whom all correspondence should be addressed.

Fibers in a flow field are subjected to a coupled motion of translation and rotation. The movement of a fiber is greatly influenced by its changing orientation in the flow field. Orientation of an ellipsoidal body in a constant-gradient flow field has been obtained by Jeffery (1923) and used by a number of investigators to determine fiber travel in various flow fields. These results are either numerical (Gallily and Eisner, 1979; Foss *et al.*, 1989) or analytical but valid only for a constant-gradient flow field (Chen and Yu, 1991a, b). Asgharian and Anjilvel (1995a) found analytical expressions for predicting fiber change of orientation in a shear flow. These results were for straight fibers, including the inertial effects on fiber orientation, and can easily be implemented to study fiber travel in an impactor.

In this study, the goal was to evaluate the characteristic behavior of impactors in separating fibers. The collection efficiencies for two types of impactor nozzles were calculated: gradual inlet nozzle and straight orifice (Jurcik and Wang, 1995). First, the flow field in one stage of the impactor was solved using a commercially available software package (FIDAP, Fluid Dynamics International, Inc., Evanston, IL U.S.A.). The flow field data were used to develop a computer program for calculating the path of travel in the impactor. By simulating a large number of paths, collection efficiency was determined. The computer program was tested by comparing the results found here for spherical particles with those in the literature. Collection efficiency curves for fibers were established as a function of fiber aspect ratio and Stokes number.

MATHEMATICAL FORMULATION

The concentration of spherical particles and fibers were assumed to be low enough not to influence the flow field. The velocity field in an impactor is axisymmetric with radial and axial components only: $\mathbf{u} = u_r \hat{e}_r + u_z \hat{e}_z$. The velocity field can be obtained by solving the Navier–Stokes and continuity equations for incompressible steady-state flow:

$$\frac{D\mathbf{u}}{Dt} = (\mathbf{u} \cdot \nabla)\mathbf{u} = -\nabla P + \nu \nabla^2 \mathbf{u}, \quad (1)$$

$$\nabla \cdot \mathbf{u} = 0, \quad (2)$$

where P is the pressure, ν is the kinematic viscosity and t is time elapsed. The flow velocities were calculated by a finite element method using FIDAP. The flow Reynolds number for gradual inlet nozzle geometry was 100 at the throat. The inlet velocity to the flow regime was assumed to be parabolic. For the straight orifice geometry, the inlet velocity to the flow regime was uniform, and the flow Reynolds number was 1100.

Movement of a fiber in a flow depends on its orientation relative to the direction of motion. The orientation of the fiber can be uniquely specified by three independent Euler angles (ϕ, θ, ψ). Two sets of coordinate systems, (x, y, z) and (x', y', z') , are used to define the Euler angles. The inertial (global) coordinate system (x, y, z) is fixed in space, and the body (local) coordinate system (x', y', z') is the set of principal axes fixed to the fiber, with x' being along the fiber length. The Euler angles describe the orientation of the two coordinate systems with respect to each other (Fig. 1). Asgharian and Anjilvel (1995a) used the fluid dynamic torque expressions found by Jeffery (1923) to derive expressions describing fiber orientation change. These equations in a cylindrical coordinate system (r, α, z) can be expressed as

$$I_{y'y'} \sin \theta \frac{d^2 \phi}{dt^2} = I_{x'x'} \frac{d\psi}{dt} \frac{d\theta}{dt} + (I_{x'x'} - 2I_{y'y'}) \cos \theta \frac{d\phi}{dt} \frac{d\theta}{dt} + \frac{8\pi\mu}{3} \frac{\beta^2 + 1}{\beta^2 \alpha_0 + \gamma_0} \\ \times \left\{ \frac{\beta^2 - 1}{\beta^2 + 1} \left[\left(\frac{\partial u_r}{\partial r} - \frac{u_r}{r} \right) \sin 2\alpha \cos \phi \cos \theta + \left(\frac{\partial u_r}{\partial z} + \frac{\partial u_z}{\partial r} \right) (\cos \alpha \cos \theta \sin \phi \right. \right.$$

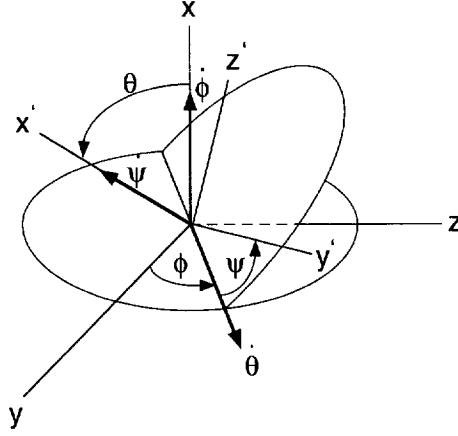


Fig. 1. Fiber orientation in a flow.

$$\begin{aligned}
 & -\sin \alpha \cos 2\phi \sin \theta) + \left(\sin^2 \alpha \frac{\partial u_r}{\partial r} + \cos^2 \alpha \frac{u_r}{r} - \frac{\partial u_z}{\partial z} \right) \sin 2\phi \sin \theta \Big] \\
 & + \left(\frac{\partial u_z}{\partial r} - \frac{\partial u_r}{\partial z} \right) (\cos \alpha \cos \theta \sin \phi + \sin \alpha \sin \theta) - 2 \sin \theta \frac{d\phi}{dt} \Big\}, \quad (3)
 \end{aligned}$$

$$\begin{aligned}
 I_{y'y'} \frac{d^2\theta}{dt^2} = & -I_{x'x'} \sin \theta \frac{d\psi}{dt} \frac{d\phi}{dt} + \frac{1}{2} (I_{y'y'} - I_{x'x'}) \sin 2\theta \left(\frac{d\phi}{dt} \right)^2 + \frac{8\pi\mu}{3} \frac{\beta^2 + 1}{\beta^2 \alpha_0 + \gamma_0} \\
 & \times \left\{ \cos \alpha \cos \phi \left(\frac{\partial u_r}{\partial z} - \frac{\partial u_z}{\partial r} \right) - 2 \frac{d\theta}{dt} - \frac{\beta^2 - 1}{\beta^2 + 1} \left[\left(\frac{\partial u_r}{\partial z} + \frac{\partial u_z}{\partial r} \right) (\cos \alpha \cos 2\theta \cos \phi \right. \right. \\
 & + \frac{1}{2} \sin \alpha \cos 2\phi \sin 2\theta) + \frac{\partial u_r}{\partial r} (-\sin 2\alpha \cos 2\theta \sin \phi + \sin 2\theta \cos^2 \alpha \\
 & - \sin 2\theta \sin^2 \phi \sin^2 \alpha) + \frac{u_r}{r} (\sin 2\alpha \cos 2\theta \sin \phi + \sin 2\theta \sin^2 \alpha \\
 & \left. \left. - \sin 2\theta \sin^2 \phi \cos^2 \alpha) - \frac{\partial u_z}{\partial z} \sin 2\theta \cos^2 \phi \right] \right\} \quad (4)
 \end{aligned}$$

$$\begin{aligned}
 I_{y'y'} \sin \theta \frac{d^2\psi}{dt^2} = & -I_{x'x'} \cos \theta \frac{d\psi}{dt} \frac{d\theta}{dt} + [(I_{y'y'} - I_{x'x'}) \cos^2 \theta + I_{y'y'}] \frac{d\phi}{dt} \frac{d\theta}{dt} \\
 & - \frac{8\pi\mu}{3} \frac{\beta^2 + 1}{\beta^2 \alpha_0 + \gamma_0} \cos \theta \left\{ \frac{\beta^2 - 1}{\beta^2 + 1} \left[\left(\frac{\partial u_r}{\partial r} - \frac{u_r}{r} \right) \sin 2\alpha \cos \phi \cos \theta \right. \right. \\
 & + \left(\frac{\partial u_r}{\partial z} + \frac{\partial u_z}{\partial r} \right) (\cos \alpha \cos \theta \sin \phi - \sin \alpha \cos 2\phi \sin \theta) \\
 & + \left. \left. \left(\sin^2 \alpha \frac{\partial u_r}{\partial r} + \cos^2 \alpha \frac{u_r}{r} - \frac{\partial u_z}{\partial z} \right) \sin 2\phi \sin \theta \right] \right. \\
 & + \left. \left(\frac{\partial u_z}{\partial r} - \frac{\partial u_r}{\partial z} \right) (\cos \alpha \cos \theta \sin \phi + \sin \alpha \sin \theta) - 2 \sin \theta \frac{d\phi}{dt} \right\} \\
 & + \frac{I_{y'y'} \sin \theta}{I_{x'x'}} \frac{16\pi\mu}{3\gamma_0} \left\{ \frac{1}{2} \left(\frac{\partial u_z}{\partial r} - \frac{\partial u_r}{\partial z} \right) (\cos \theta \sin \alpha - \cos \alpha \sin \phi \sin \theta) \right. \\
 & \left. - \frac{d\psi}{dt} - \frac{d\phi}{dt} \cos \theta \right\}, \quad (5)
 \end{aligned}$$

where μ is the air viscosity, β is fiber aspect ratio, $I_{x'x'}$ and $I_{y'y'}$ are the components of the moment of inertia tensor of the fiber about its center (Asgharian and Anjilvel, 1995b), and α_0 and γ_0 are parameters related to fiber geometry (Gallily and Cohen, 1979).

A fiber travelling through an impactor experiences only a drag force, \mathbf{F}_D , which opposes its motion. The governing equation of motion can be written as

$$\mathbf{F}_D = \frac{\rho\pi d_f^3\beta}{6} \mathbf{a}, \quad (6)$$

where d_f is fiber diameter, \mathbf{a} is the acceleration of the center of the fiber and

$$\mathbf{F}_D = 3\pi\mu[\mathbf{A}] \begin{bmatrix} d_{\parallel} & 0 & 0 \\ 0 & d_{\perp} & 0 \\ 0 & 0 & d_{\perp} \end{bmatrix} [\mathbf{A}]^{-1}(\mathbf{u} - \mathbf{u}_p) \quad (7)$$

in which d_{\parallel} and d_{\perp} are the Stokes diameters when the fiber is parallel and perpendicular to the flow direction (Gans, 1928), \mathbf{u}_p is the velocity of the fiber, and $[\mathbf{A}]$ is the transformation matrix from the local to the global coordinate system (Asgharian and Anjilvel, 1995b). By replacing equation (7) for \mathbf{F}_D into equation (6) and simplifying, the following set of equations are obtained:

$$\begin{aligned} \frac{d^2r}{dt^2} = & \frac{1}{\tau} \left\{ \left[\left(\frac{d_{\parallel}}{d_f} - \frac{d_{\perp}}{d_f} \right) (\cos^2\theta \cos^2\alpha + \sin^2\phi \sin^2\theta \sin^2\alpha + \frac{1}{2}\sin\phi \sin 2\theta \sin 2\alpha) + \frac{d_{\perp}}{d_f} \right] \right. \\ & \times \left(u_r - \frac{dr}{dt} \right) + \frac{1}{2} \left(\frac{d_{\parallel}}{d_f} - \frac{d_{\perp}}{d_f} \right) (\cos^2\theta \sin 2\alpha - \sin^2\phi \sin^2\theta \sin 2\alpha \\ & - \sin\phi \sin 2\theta \cos 2\alpha) r \frac{d\alpha}{dt} - \frac{1}{2} \left(\frac{d_{\parallel}}{d_f} - \frac{d_{\perp}}{d_f} \right) (\cos\phi \sin 2\theta \cos\alpha \\ & \left. + \sin^2\theta \sin 2\phi \sin\alpha) \left(u_z - \frac{dz}{dt} \right) \right\} + r \left(\frac{d\alpha}{dt} \right)^2, \quad (8) \end{aligned}$$

$$\begin{aligned} \frac{d^2\alpha}{dt^2} = & \frac{1}{r\tau} \left\{ \frac{1}{2} \left(\frac{d_{\parallel}}{d_f} - \frac{d_{\perp}}{d_f} \right) (\cos^2\theta \sin 2\alpha - \sin^2\phi \sin^2\theta \sin 2\alpha - \sin\phi \sin 2\theta \cos 2\alpha) \right. \\ & \times \left(\frac{dr}{dt} - u_r \right) + \left[\left(\frac{d_{\parallel}}{d_f} - \frac{d_{\perp}}{d_f} \right) \left(\frac{1}{2} \sin\phi \sin 2\theta \sin 2\alpha - \sin^2\phi \sin^2\theta \cos^2\alpha \right. \right. \\ & \left. \left. - \cos^2\theta \sin^2\alpha \right) - \frac{d_{\perp}}{d_f} \right] r \frac{d\alpha}{dt} + \frac{1}{2} \left(\frac{d_{\parallel}}{d_f} - \frac{d_{\perp}}{d_f} \right) (\cos\phi \sin 2\theta \sin\alpha \\ & \left. - \sin^2\theta \sin 2\phi \cos\alpha) \left(u_z - \frac{dz}{dt} \right) \right\} - \frac{2}{r} \frac{dr}{dt} \frac{d\alpha}{dt}, \quad (9) \end{aligned}$$

$$\begin{aligned} \frac{d^2z}{dt^2} = & \frac{1}{\tau} \left\{ \frac{1}{2} \left(\frac{d_{\parallel}}{d_f} - \frac{d_{\perp}}{d_f} \right) (\cos\phi \sin 2\theta \cos\alpha + \sin^2\theta \sin 2\phi \sin\alpha) \left(\frac{dr}{dt} - u_r \right) \right. \\ & - \frac{1}{2} \left(\frac{d_{\parallel}}{d_f} - \frac{d_{\perp}}{d_f} \right) (\cos\phi \sin 2\theta \sin\alpha - \sin^2\theta \sin 2\phi \cos\alpha) r \frac{d\alpha}{dt} \\ & \left. + \left[\left(\frac{d_{\parallel}}{d_f} - \frac{d_{\perp}}{d_f} \right) \cos^2\phi \sin^2\theta + \frac{d_{\perp}}{d_f} \right] \left(u_z - \frac{dz}{dt} \right) \right\}, \quad (10) \end{aligned}$$

where $\tau = \rho d_f^2 \beta / 18\mu$. Equations (3)–(5) and (8)–(10) can be nondimensionalized using the impactor throat diameter, D , and the average velocity through the throat, U . The non-dimensional form of the equations depends on two nondimensional parameters: fiber aspect ratio, β , and fiber Stokes number, $\text{Stk} = \rho d_f^2 \beta U / 18\mu D$. Despite an axisymmetric flow field, fibers, can travel in α direction and thus equations (8)–(10) have to be solved to determine fiber trajectory.

If $d_{\parallel} = d_{\perp}$ in equations (8)–(10), equations of motion for spherical particles are obtained:

$$\frac{d^2 r}{dt^2} = r \left(\frac{d\alpha}{dt} \right)^2 + \frac{1}{\tau} \left(u_r - \frac{dr}{dt} \right), \quad (11)$$

$$\frac{d^2 \alpha}{dt^2} = -\frac{2}{r} \frac{d\alpha}{dt} \frac{dr}{dt} - \frac{1}{\tau} \frac{d\alpha}{dt}, \quad (12)$$

$$\frac{d^2 z}{dt^2} = \frac{1}{\tau} \left(u_z - \frac{dz}{dt} \right). \quad (13)$$

Equations (11)–(13) in nondimensional form are only a function of spherical particle Stokes number, $Stk = \rho d^2 U / 18 \mu D$, in which d is the spherical particle diameter.

The set of equations (3)–(5) and (8)–(10) for fibers is converted into a set of 12 first-order equations. Similarly, the set of equations (11)–(13) for spherical particles are converted into a set of six first-order equations. These sets of first order equations are solved numerically using a fourth-order Runge–Kutta method by adopting a variable time step. Flow field data obtained from the solution of the Navier–Stokes equations are used in these equations, and the trajectories of spherical particles and fibers are obtained. The finite element solution of Navier–Stokes equations gives numerical values of the velocity field at discrete points (nodal points of an element) in the domain. A technique described in Appendix A is used to locate the spherical particle or fiber in the flow domain and calculate the velocity at its current position (see also Asgharian and Anjilvel, 1994). To calculate fiber orientation, velocity gradients at the nodal points of the finite element domain are calculated using the method presented in Appendix B.

Fibers and spherical particles are assumed to enter the impactor at zero initial velocity and uniform inlet concentration. The trajectories of spherical particles and fibers of different sizes starting at various inlet positions were calculated. If a spherical particle reaches a distance of its radius from the wall, it is assumed to deposit. Fibers deposit when one tip of a fiber touches a wall (Appendix C). Using the limiting trajectory method (Pich, 1972), the collection efficiency of spherical particles and fibers is calculated. Collection efficiency is the fraction of entering spherical particles or fiber that deposit on the impaction plate.

RESULTS AND DISCUSSION

FIDAP was used to calculate the flow field for the two nozzle geometries. The meshing for the two geometries is shown in Fig. 2. The mesh consisted of 9626 elements and 9348 nodal points for the gradual inlet nozzle and 11,756 elements and 11,458 nodal points for the straight orifice. Very fine grading near the impaction plates was used since flow has very large velocity gradients in this region.

Since there are no useful experimental data for fibers, the model was compared with two other model calculations for spherical particles. One model has been tested against experimental data. Jurcik and Wang (1995) tested their model with data of Wang and John (1988) and Hillamo and Kauppinen (1991) and found very good agreement between numerical calculations and experimental results. We compared our collection efficiency results with those of Jurcik and Wang (1995) and Rader and Marple (1985) in an impactor with gradual inlet geometry. The results are presented in Fig. 3. The comparison was made at a flow Reynolds number of 100 with identical geometrical dimensions. The present results showed trends in the shape and magnitude of the collection efficiency curve similar to those of Jurcik and Wang (1995). Particle cutoff size at 50% efficiency was near $\sqrt{Stk} = 0.31$ for both studies. Both analyses used FIDAP for the flow field calculations. The calculated collection efficiencies were smaller than those of Rader and Marple (1985), who used a finite difference method to calculate the flow field.

The above geometry was also used to study fiber separation at a Reynolds number of 100. The calculated trajectories of a unit density fiber with $d_f = 2 \mu\text{m}$ and $\beta = 10$ released at

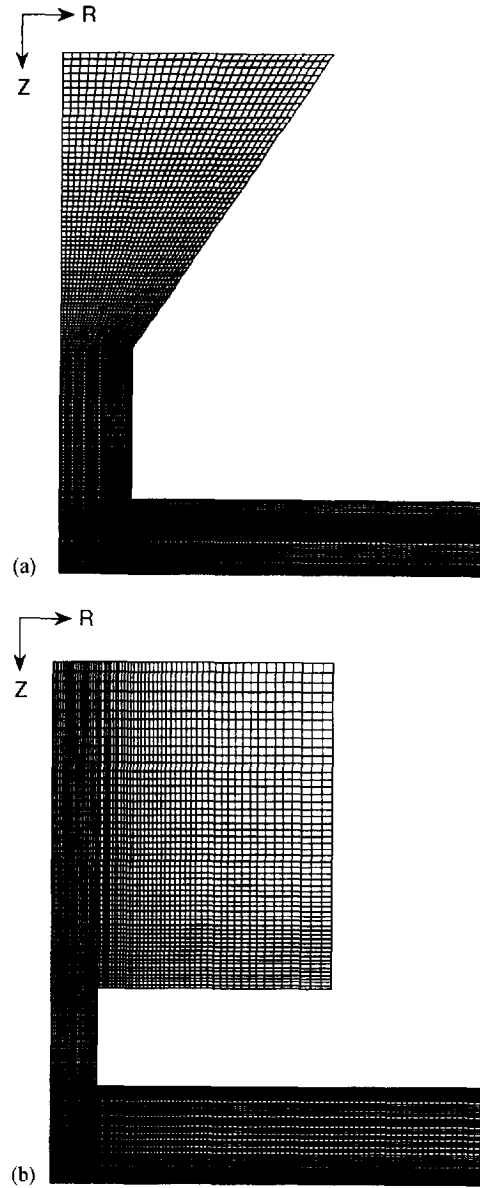


Fig. 2. Finite element mesh of the geometry: (a) gradual inlet nozzle with 9626 elements and 9348 nodes; (b) straight orifice with 11,756 elements and 11,458 nodes.

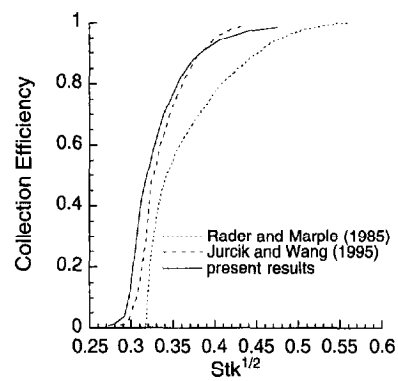


Fig. 3. Comparison of the calculated collection efficiency for spherical particles with that of other investigators. The flow Reynolds number is 100.

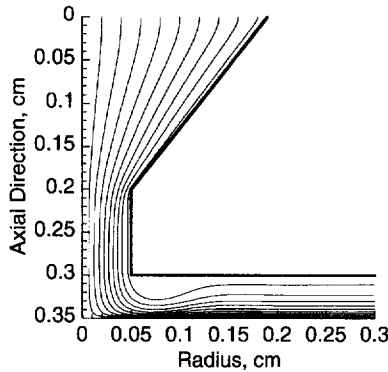


Fig. 4. Trajectories of a unit density fiber with $d_f = 2 \mu\text{m}$, $\beta = 10$ in a gradual inlet nozzle for a Reynolds number of 100.

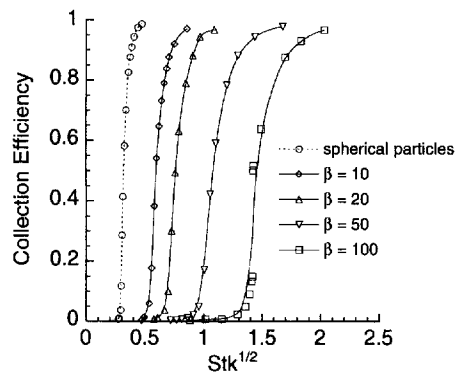


Fig. 5. Calculated collection efficiency of spherical particles and fibers in a gradual inlet nozzle for a Reynolds number of 100.

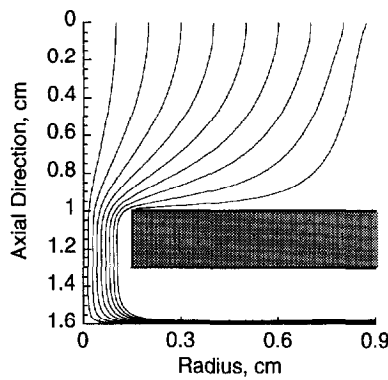
different starting positions with zero initial velocity and initial orientation angles $\phi = \theta = 45^\circ$, $\psi = 0$ are shown in Fig. 4. All the trajectories shown exited the impactor. The trajectories had trends similar to those for spherical particles given by Jurcik and Wang (1995). Similar to spherical particles, fibers underwent aerodynamic focusing (Rao *et al.*, 1993) since most of the trajectories ended up near the impaction plate, illustrating that fibers can also be separated by their Stokes numbers.

Equations (3)–(5) and (8)–(10) show that fiber deposition depends on its Stokes number and aspect ratio. The effect of initial orientation was found not to be significant since the fibers entering the throat tend to align to the flow and redistribute their orientations as they turn to exit the impactor. The results of fiber collection efficiency calculations as a function of Stokes number and aspect ratio are shown in Fig. 5. The results for spherical particles are also shown for the sake of comparison. The Stokes number at the 50% cutoff size increased, as the fiber aspect ratio increased, but the calculated cutoff size diameter of the fiber decreased. Similar to experimental results, the tails of the collection efficiency curves increased at the low-efficiency end. For fibers, there was a 2–3% loss on the side walls, and thus the collection efficiency curve never reached 100%. The cutoff size of spherical particles and fibers for this case is presented in Table 1.

Calculations were also performed for a straight-orifice nozzle with dimensions and flow rates similar to those of the second stage of a Mercer impactor (In-Tox Products, Albuquerque, NM). The second stage of a Mercer impactor has two nozzles with straight-orifice geometry and 0.3 cm diameter. Flow through the second stage is 5 l min^{-1} , which corresponds to a Reynolds number of 1100. The trajectories of a unit density fiber with $d_f = 1 \mu\text{m}$ and $\beta = 10$ starting at different inlet positions are shown in Fig. 6. Inlet flow was assumed to

Table 1. Calculated cutoff size of spherical particles and fibers

Aspect ratio	Diameter at 50% efficiency	
	Gradual inlet nozzle	Straight orifice
1	4.70	4.19
10	2.77	2.44
20	2.50	2.18
50	2.25	1.94
100	2.10	1.82

Fig. 6. Trajectories of a unit density fiber with $d_f = 1 \mu\text{m}$, $\beta = 10$ in a straight-orifice geometry for a Reynolds number of 1100.

be uniform and fibers entered with zero initial velocity and initial orientation $\phi = \theta = 45^\circ$, $\psi = 0$. All the trajectories simulated got very close to the impaction plate, although none deposited. The trajectories were also similar to those of spherical particles as calculated here (not shown) and by Jurcik and Wang (1995). One noticeable difference, however, was the loss of about 9% of fibers on the side wall of the throat, as shown in Fig. 6 by the trajectory of a fiber starting at a radius of 0.87 cm.

The corresponding collection efficiency curves for spherical particles and fibers are shown in Fig. 7. The shapes of the collection efficiency curves are more like a step function than an S-shaped curve, particularly for spherical particles. The 50% cutoff size for spherical particles is at $4.19 \mu\text{m}$, which is in excellent agreement with the measured value of $4.12 \mu\text{m}$ (operation manual, In-Tox Products, Albuquerque, NM). Fibers show a long tail at the low-efficiency end of the curves consistent with experimental observations but no tail at the high-efficiency end since collection efficiency never reaches 100%. This is because spherical particles and fibers that are released at the upper end of the impactor inlet are deposited on the side wall of the throat. The loss can approach 9%. A similar trend is also observed in the results of Jurcik and Wang (1995) for spherical particles. The cutoff diameters at 50% collection efficiency corresponding to this case are also tabulated in Table 1.

Fiber Stokes number and hence collection efficiency depend on both diameter and length of the fiber. Thus inertial separation of fibers cannot be found as a function of diameter only. To show this, collection efficiency of the second stage of the Mercer-type impactor is plotted against its length and diameter in Fig. 8. Fibers smaller than $2 \mu\text{m}$ diameter showed little deposition. At $2 \mu\text{m}$ diameter, collection efficiency increased with length, showing that length can also be significant for collection efficiency. Thus separation characteristics should be considered in terms of two parameters (e.g. Stokes number and aspect ratio) when separating fibers using an impactor, rather than in terms of geometric or aerodynamic diameter alone.

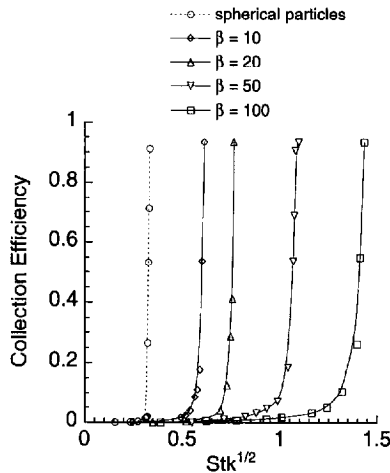


Fig. 7. Calculated collection efficiency of spherical particles and fibers in a straight-orifice geometry for a Reynolds number of 1100.

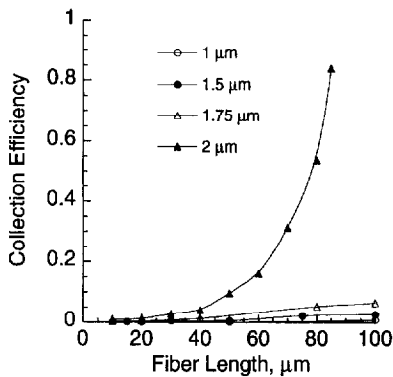


Fig. 8. Calculated collection efficiency of fiber as a function of length and diameter.

CONCLUSIONS

Impactors of various nozzle geometries can be used for the size characterization of particles and fibers. In this study, collection efficiencies of spherical particles and fibers for two types of impactors were calculated. The cutoff size at 50% efficiency was in agreement with experimental data and numerical results from other investigators. The collection efficiency of fibers was characterized in terms of fiber Stokes number and aspect ratio. As the fiber aspect ratio increased and the cutoff size diameter of the fiber decreased, the fiber collection efficiency curve for fibers moved to a higher Stokes number.

Acknowledgements—This work was supported in part by grants from the North American Insulation Manufacturers Association and the Refractory Ceramic Fiber Coalition and in part by Grant No. KO1-OH00129 from NIOSH. The authors are also grateful to Dr Barbara Kuyper for her editorial assistance in the preparation of this manuscript.

REFERENCES

- Asgharian, B. and Anjilvel, S. (1994) *Aerosol Sci. Technol.* **20**, 177.
 Asgharian, B. and Anjilvel, S. (1995a) *Aerosol Sci. Technol.* **23**, 282.
 Asgharian, B. and Anjilvel, S. (1995b) *Aerosol Sci. Technol.* **22**, 261.
 Chen, Y. K. and Yu, C. P. (1991a) *Aerosol Sci. Technol.* **14**, 343.
 Chen, Y. K. and Yu, C. P. (1991b) *J. Aerosol Sci.* **22**, 747.
 Davis, C. N. and Aylward, M. (1951) *Proc. Phys. Soc. (London)* **B64**, 889.

- Esmen, N. A. and S. Erdal (1991) *Appl. Occup. Environ. Hyg.* **6**, 764.
 Foss, J. M., Frey, M. F., Schamberger, M. R., Peters, J. E. and Leong, K. H. (1989) *J. Aerosol Sci.* **20**, 515.
 Gallily, I. and Cohen, A. (1979) *J. Colloid Interface Sci.* **68**, 338.
 Gallily, I. and A. D. Eisner (1979) *J. Colloid Interface Sci.* **68**, 320.
 Gans, K. R. (1928) *Ann. Phys.* **86**, 628.
 Hillamo, R. E. and Kauppinen, E. I. (1991) *Aerosol Sci. Technol.* **14**, 3.
 Jeffery, G. B. (1923) *Proc. Roy. Soc. Lond.* **A102**, 161.
 Jurcik, B. and Wang, H. C. (1995) *J. Aerosol Sci.* **26**, 1139.
 Marple, V. A. (1970) Ph.D. thesis, Mechanical Engineering Department, University of Minnesota, Particle Technology Laboratory Publication No. 144.
 Marple, V. A., Liu, B. Y. H. and Whitby, K. (1974) *Aerosol Sci.* **5**, 1.
 Mercer, T. T. and Chow, H. Y. (1968) *J. Colloid Interface Sci.* **27**, 75.
 Mercer, T. T. and Stafford, R. G. (1969) *Ann. Occup. Hyg.* **12**, 41.
 Pich, J. (1972) *J. Aerosol Sci.* **3**, 351.
 Rader, D. J. and Marple, V. A. (1985) *Aerosol Sci. Technol.* **4**, 141.
 Ranz, W. E. and Wong, J. B. (1952) *Ind. Engng. Chem.* **44**, 1371.
 Rao, N. P., Navascues, J. and Fernandez De La Mora, J. (1993) *J. Aerosol Sci.* **24**, 879.
 Wang, H. C. and John, W. (1988) *Aerosol Sci. Technol.* **8**, 157.
 Wilcox, J. D. (1953) *A.M.A. Arch. Ind. Hyg. Occup. Med.* **7**, 376.
 Yu, C. P., Asgharian, B. and Yen, B. M. (1986) *Am. Ind. Hyg. Assoc. J.* **47**, 72.

APPENDIX A

FIDAP calculates flow velocities at four nodal points of an element (axisymmetric flow in two directions). By assumption, any flow property (such as velocity) in the element varies linearly with position. To locate a spherical particle or fiber inside an element, the element is mapped linearly from geometric coordinates (r, z) to integer domain (ξ, η) with $0 \leq \xi \leq 1$ and $0 \leq \eta \leq 1$.

$$r = C_{r1} + C_{r2}\xi + C_{r3}\eta + C_{r4}\xi\eta, \quad (\text{A1})$$

$$z = C_{z1} + C_{z2}\xi + C_{z3}\eta + C_{z4}\xi\eta, \quad (\text{A2})$$

where $C_{r1} - C_{r4}$ and $C_{z1} - C_{z4}$ are constant coefficients for each element found by replacing (r, z) and (ξ, η) values at the nodal points of the element in equations (A1) and (A2).

$$r = r_1 + (r_2 - r_1)\xi + (r_4 - r_1)\eta + (r_1 - r_2 + r_3 - r_4)\xi\eta, \quad (\text{A3})$$

$$z = z_1 + (z_2 - z_1)\xi + (z_4 - z_1)\eta + (z_1 - z_2 + z_3 - z_4)\xi\eta. \quad (\text{A4})$$

For a given value of (r, z), equations (A3) and (A4) are solved simultaneously for ξ and η . If values of ξ and η fall between 0 and 1, the spherical particle or fiber is inside the element. Using the calculated values of (ξ, η), the velocity field in that position is found by a set of equations similar to (A3) and (A4).

$$u_r = u_{r1} + (u_{r2} - u_{r1})\xi + (u_{r4} - u_{r1})\eta + (u_{r1} - u_{r2} + u_{r3} - u_{r4})\xi\eta, \quad (\text{A5})$$

$$u_z = u_{z1} + (u_{z2} - u_{z1})\xi + (u_{z4} - u_{z1})\eta + (u_{z1} - u_{z2} + u_{z3} - u_{z4})\xi\eta. \quad (\text{A6})$$

APPENDIX B

Fiber orientation depends on velocity gradients in the flow. Since FIDAP only gives velocity values at the nodal points of the element, velocity gradients have to be calculated from velocity values. All the calculations are performed in integer domain. For a fiber located inside an element, the following equations hold for the radial component of the velocity:

$$\frac{\partial u_r}{\partial r} = \frac{\partial u_r}{\partial \xi} \frac{\partial \xi}{\partial r} + \frac{\partial u_r}{\partial \eta} \frac{\partial \eta}{\partial r}, \quad (\text{B1})$$

$$\frac{\partial u_r}{\partial z} = \frac{\partial u_r}{\partial \xi} \frac{\partial \xi}{\partial z} + \frac{\partial u_r}{\partial \eta} \frac{\partial \eta}{\partial z}. \quad (\text{B2})$$

By differentiating equations (A1) and (A2) with respect to ξ and η and solving, quantities $\partial \xi / \partial r$, $\partial \xi / \partial z$, $\partial \eta / \partial r$, and $\partial \eta / \partial z$ are found. By substituting for these values and velocity gradients in integer domain at each nodal points, velocity gradients are obtained.

At node (1):

$$\frac{\partial u_r}{\partial r} = \frac{(z_4 - z_1)(u_{r2} - u_{r1}) - (z_2 - z_1)(u_{r4} - u_{r1})}{r_2(z_4 - z_1) - z_2(r_4 - r_1)}, \quad (\text{B3})$$

$$\frac{\partial u_r}{\partial z} = \frac{-(r_4 - r_1)(u_{r2} - u_{r1}) + (r_2 - r_1)(u_{r4} - u_{r1})}{r_2(z_4 - z_1) - z_2(r_4 - r_1)}. \quad (\text{B4})$$

At node (2):

$$\frac{\partial u_r}{\partial r} = \frac{(z_3 - z_2)(u_{r2} - u_{r1}) - (z_2 - z_1)(u_{r3} - u_{r1})}{z_3(r_2 - r_1) + z_2(r_1 - r_3) + z_1(r_3 - r_2)}, \quad (\text{B5})$$

$$\frac{\partial u_r}{\partial z} = \frac{-(r_3 - r_2)(u_{r2} - u_{r1}) + (r_2 - r_1)(u_{r3} - u_{r1})}{z_3(r_2 - r_1) + z_2(r_1 - r_3) + z_1(r_3 - r_2)}. \quad (\text{B6})$$

At node (3):

$$\frac{\partial u_r}{\partial r} = \frac{(z_3 - z_2)(u_{r3} - u_{r4}) - (z_3 - z_4)(u_{r3} - u_{r2})}{z_2(r_4 - r_3) + z_3(r_2 - r_4) + z_4(r_3 - r_2)}, \quad (\text{B7})$$

$$\frac{\partial u_r}{\partial z} = \frac{-(r_3 - r_2)(u_{r3} - u_{r4}) + (r_3 - r_4)(u_{r3} - u_{r2})}{z_2(r_4 - r_3) + z_3(r_2 - r_4) + z_4(r_3 - r_2)}. \quad (\text{B8})$$

At node (4):

$$\frac{\partial u_r}{\partial r} = \frac{(z_4 - z_1)(u_{r3} - u_{r4}) - (z_3 - z_4)(u_{r4} - u_{r1})}{z_1(r_4 - r_3) + z_3(r_1 - r_4) + z_4(r_3 - r_1)}, \quad (\text{B9})$$

$$\frac{\partial u_r}{\partial z} = \frac{-(r_4 - r_1)(u_{r3} - u_{r4}) + (r_3 - r_4)(u_{r4} - u_{r1})}{z_1(r_4 - r_3) + z_3(r_1 - r_4) + z_4(r_3 - r_1)}. \quad (\text{B10})$$

Velocity gradients for the z component of the velocity are found by replacing u_z for u_r in equations (B2)–(B10).

Once velocity gradients are determined at nodal points, the method in Appendix A can be employed to calculate velocity gradients at any point in the flow domain.

APPENDIX C

When the center of a spherical particle or fiber reaches within one radius from a wall, it deposits. If a wall element is represented by nodal points (1) and (2), and the spherical particle or fiber current position is at (r, z) , its distance from the wall is

$$H = \frac{1}{2h_3} \sqrt{[h_2^2 - (h_1 - h_3)^2][(h_1 + h_3)^2 - h_2^2]}, \quad (\text{C1})$$

where

$$h_1 = \sqrt{(r - r_1)^2 + (z - z_1)^2}, \quad (\text{C2})$$

$$h_2 = \sqrt{(r - r_2)^2 + (z - z_2)^2}, \quad (\text{C3})$$

$$h_3 = \sqrt{(r_1 - r_2)^2 + (z_1 - z_2)^2}. \quad (\text{C4})$$

For $H \leq d/2$ or $H \leq d_f/2$, spherical particle or fiber deposits.

Additionally, a fiber deposits when a tip of a fiber touches a wall. At a position when a tip has touched the wall, the fiber is at a distance H' from the wall:

$$H' = \frac{1}{2H} \left[\left(\frac{l_p}{2} \right)^2 + H^2 - h_4^2 \right]. \quad (\text{C5})$$

where

$$l_p = l_f \sqrt{1 - \sin^2 \phi \sin^2 \theta}, \quad (\text{C6})$$

$$h_4 = \sqrt{(r_t - r_h)^2 + (z_t - z_h)^2} \quad (\text{C7})$$

in which l_f is fiber length, (r_t, z_t) are the coordinates of the tip of the fiber, and (r_h, z_h) are the coordinates of the center of the fiber projected on the wall.

$$r_t = r \pm \frac{l_f}{2} \cos \theta, \quad (\text{C8})$$

$$z_t = z \mp \frac{l_f}{2} \sin \theta \cos \phi \quad (\text{C9})$$

$$r_h = \frac{(r_2 - r_1)[r(r_2 - r_1) + (z - z_1)(z_2 - z_1)] + r_1(z_2 - z_1)^2}{(r_2 - r_1)^2 + (z_2 - z_1)^2}, \quad (\text{C10})$$

$$z_h = \frac{(r_2 - r_1)[z_1(r_2 - r_1) + (r - r_1)(z_2 - z_1)] + z(z_2 - z_1)^2}{(r_2 - r_1)^2 + (z_2 - z_1)^2}, \quad (\text{C11})$$

For $H \leq H'$, fibers deposit on the wall.